Construction and Building Materials 229 (2019) 117102

Contents lists available at ScienceDirect

Construction and Building Materials

journal homepage: www.elsevier.com/locate/conbuildmat

Reinforced concrete mapping using full-waveform inversion of GPR data

Sajad Jazayeri [a,*], Sarah Kruse [a], Istiaque Hasan [b], Nur Yazdani [c]

[a] School of Geosciences, University of South Florida, Tampa, FL 33620, USA
[b] Pennoni Associates Inc., Philadelphia, PA 19103, USA
[c] Department of Civil Engineering, University of Texas at Arlington, TX 76019, USA

ARTICLE INFO

Article history:
Received 27 March 2019
Received in revised form 16 September 2019
Accepted 27 September 2019

Keywords:
Ground penetrating radar
Rebar
Reinforced concrete
Utilities
Full-waveform inversion
Deconvolution
Sparsity

ABSTRACT

Mapping the location and dimension of reinforcing bars in concrete can be critical for assessing the structure and state of reinforced concrete. Concrete structures, such as bridge pilings or cell phone tower foundations, are integral to modern life. Ground penetrating radar (GPR) is commonly used for mapping rebar grids, but traditional GPR data processing techniques fail to provide reliable information on the diameter of bars. Full-waveform inversion (FWI) of surface-coupled common-offset GPR B-scans (profiles) over reinforced concrete improves estimates of rebar diameters over more conventional ray-based methods. The method applies a sparse blind deconvolution (SBD) technique to obtain the optimized source wavelet and a sparse representation of the subsurface reflectivity series. A ray-based analysis is then performed on the estimated reflectivity model to define the initial geometry model to start the FWI. Applying this method to a synthetic data set and two real data cases with 1 and 2.6 GHz center frequency antennas results in errors in the rebar diameter estimates of less than 11% for rebars with concrete cover of 7.5 cm or less. These results compare favorably with those obtained from other methods that require cross-polarized antennas or ancillary equipment. The synthetic model demonstrates that the combination of SBD and FWI also improves ray-based estimates of the concrete permittivity and conductivity.

1. Introduction

Ground penetrating radar (GPR) is a non-invasive, exploratory tool widely applied to mapping reinforcing bars embedded in concrete (e.g. [1–5]). As a GPR system is towed over concrete, high frequency electromagnetic (EM) pulses are emitted by a transmitting antenna. These pulses reflect off reinforcing bars, and are recorded at a receiving antenna. Data with high spatial density can be acquired at driving speeds, with obvious benefits for road and bridge deck monitoring [1].

GPR returns depend on the material properties of the concrete and reinforcing bars, specifically the dielectric constant (i.e. relative permittivity, defined as the ratio of the electrical permittivity of the media to that of free space) and electrical conductivity. Because reinforcing bars are so distinctly different than surrounding concrete, they strongly reflect the EM energy and generate characteristic hyperbolic returns on GPR profiles, or B-scans (e.g. Fig. 1). The shape and position of a hyperbola on a GPR profile is controlled by the depth and properties of the rebar, as well as the overlying concrete properties.

1.1. Rebar position

The problem of locating the top of a bar (both laterally and in depth below concrete surface) from the arrival times of the peaks in the hyperbolic GPR return is relatively straightforward and is widely applied. A theoretical best fit curve to the hyperbola arrival times is used to estimate the velocity of the wave in the overlying concrete and thereby estimate the depth of the rebar (e.g. [3]). This calculation, referred to as ray-based analysis because it uses the travel times of selected ray paths, is typically satisfactory for studies "mapping" the locations of rebars. However, the position estimates can be biased by human errors while fitting the hyperbolas and by noise (e.g. [6,7]), and more accuracy may be desirable for more quantitative assessments or studies monitoring changes.

1.2. Rebar diameter

In contrast to the depth, the diameter of a bar is quite difficult to estimate when the diameter is small compared to the radar wavelength. With wavelengths greater than bar diameter, the arrival times of the peak returns in the hyperbola are simply relatively insensitive to the diameter. Such is commonly the case in concrete

* Corresponding author.
E-mail address: sjazayeri@mail.usf.edu (S. Jazayeri).

https://doi.org/10.1016/j.conbuildmat.2019.117102
0950-0618/

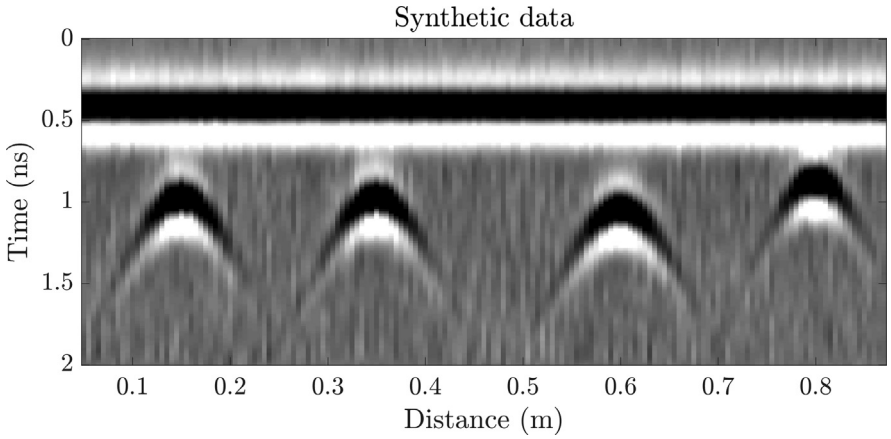

Fig. 1. Synthetic GPR returns from four reinforcing bars embedded in concrete at depths ranging from 2.7 to 4 cm, as shown in Fig. 3, assuming a 2.4 GHz center frequency antenna and the source wavelet shown in Fig. 4. Noise is added to the data to make the scenario more realistic.

investigations, where bar diameter may be 1 cm, while radar wavelength in concrete is 5.5 cm, for example for a 2.6 GHz center frequency antenna in concrete with a relative permittivity of 5. This leaves diameter estimations based on arrival times vulnerable to uncertainties in the material properties of the rebar and the overlying concrete, the shape of the pulse, and to noise in the data. In this paper we focus on a method for improving estimates of the diameters of reinforcing bars. Because this cannot be done without simultaneous estimates of the concrete properties and the GPR pulse, we describe those results as well.

To get beyond the insensitivity of longer-wavelength radar signals to small-diameter bars, a variety of methods have been proposed. These methods use more than the arrival time of GPR peak hyperbolic returns, or use ancillary data. A summary of these methods is described here, with their strengths and limitations.

Migration is a process for collapsing the diffraction hyperbolas back to their originating point, which in theory could help resolve a rebar diameter. However, in real problems, this method is not effective for improved diameter estimation [8]. Soldovieri et al. [9] propose a linear inverse scattering tomographic reconstruction algorithm in the frequency domain based on the Born Approximation. The authors claim satisfactory and reliable results in terms of localization, sizing and shape of the buried objects, but they do not provide estimates of the errors in the method.

Examining the amplitudes of the hyperbolic GPR returns may also qualitatively improve an estimate of rebar diameter. Hasan and Yazdani [10] find an approximate linear relationship between the embedded bar diameter and the maximum GPR amplitude. However, without knowledge of the source wavelet amplitude (which varies with instrument, concrete conditions, and surface contact) and concrete and rebar properties, the hyperbola peak amplitude cannot be related quantitatively to rebar diameter.

Several research groups have established experimental relationships between the amplitude and frequency content of the hyperbolic returns and the diameters of embedded bars, as well as additional properties of the rebar and concrete [11–14]. However, the primary goal of these studies is to assess corrosion and deterioration in reinforced concrete, not quantitative assessment of diameter resolution.

Researchers have also considered the amplitude ratios of the rebar returns from instrument setups with the transmitting and receiving antennas parallel each other (co-polarized), and setups with two antennas perpendicular to each other (cross-polarized) [15,16]. Regressions are used to establish experimental relationships between rebar diameter and the amplitude ratios. Leucci [16] reports an improvement on the method of Utsi and Utsi [15] can generate diameter values with 6% error. Improved diameter estimates using cross-polarized antennas are also described by Zanzi and Arosio [17], who investigate the effect of antenna polarity in rebar detection problems and also the qualitative relationships between the antenna frequency and the diameter. However, methods that require cross-polarized data are not readily available with typical commercial equipment that fixes the antenna pair in a co-polarized geometry. The amplitude ratio methods may also be sensitive to noise since absolute amplitude values are used.

Other investigators have described the results of combining GPR technology with a different commercial EM-based system for detecting rebars, a handheld concrete pachometer [18]. They report diameter estimates with 12% error. This dual method, however lacks the advantage of GPR alone, which can be towed at vehicle speeds over concrete.

In summary, there is no clearly documented method for extracting reliable diameter estimates for reinforcing bars from GPR data alone, acquired with typical commercial systems with co-polarized antennas.

1.3. Full waveform inversion (FWI)

In this paper, we address this knowledge gap by testing the method of full-waveform inversion to the rebar diameter problem. With FWI, the full waveforms of GPR traces are used, rather than simply peak arrival times. Improvements in the resolution of buried features with FWI have also been demonstrated dramatically for seismic wave studies in both oil exploration (e.g. [19–22]) and engineering applications, from foundations to sinkholes (e.g. [23–27].

FWI has been applied to the problems of concrete properties (e.g. [11,12]) and of buried pipe diameters [28,7,29]. In the latter, FWI is shown to improve diameter estimations of water or air-filled PVC pipes and also to predict the pipe's infilling material permittivity. Here, we extrapolate the methods developed for the pipe diameter problem to the resolution of rebar diameters. We explore the capabilities of the method on one synthetic and two real data sets.

Because FWI requires a starting model, it begins with a ray-based estimate of rebar diameter. To optimize this initial estimate, we derive the mathematical expression for the hyperbolic pattern of a cylindrical target perpendicular to the GPR profile, considering both target diameter and transmitter-receiver offset. Second, we adapt the FWI approach from Jazayeri et al. [7] to the problem of reinforced concrete, with the simplification that we assume to

know the electrical properties of the metallic rebar and keep them as constant parameters during the process. This approach requires the shape of the transmitted pulse (known as source wavelet or SW) as an input. We use Jazayeri et al.'s [30] Sparse Blind Deconvolution (SBD) technique to calculate the SW. Finally, we explore the capabilities of the proposed method on one synthetic and two real data sets.

2. Materials and methods

2.1. Analytical expression for travel times

The diameter of a diffracting cylinder affects the arrival time of the GPR signal and the general shape of the diffraction hyperbolas (although as described above this effect is small when the cylinder is small). Al-Nuaimy et al. [31] and Shihab et al. [32] provide formulations that consider the radius of the target and are suitable for least squares approximations. However, for simplification, they treat the transmitter-receiver offset as negligible.

Here we relax the zero-offset assumption in the ray formulation. In commercial shielded instruments the transmitting and receiving antennas move together with a constant, but non-zero, offset. Fig. 2 illustrates the problem. The transmitting (T) and receiving (R) antennas are respectively at distances d_T and d_R from the point of beam incidence on the rebar circumference (O') and are placed at x_T and x_R on ground, where $|x_T - x_R| = \delta x$ is the antenna offset. The rebar with radius r is at horizontal location x and the top of it is at depth y below the surface. Since rebar are often metallic and can be considered as almost perfect electrical conductors, the point of incidence, O' at depth $h \geqslant y$ and at horizontal location x_0, plays a critical role in shaping the hyperbolic patterns.

Antennas used in rebar inspection generally have frequencies greater than 1 GHz (due to shallow burial depth and small rebar diameters) and are very small in size (less than several centimeters). Previous authors approximated d_T and d_R as O' leading to Eq. (1). However, for small targets this approximation may approach the time corrections associated with the target radius. Here d_T and d_R are considered explicitly. To calculate d_T and d_R requires O' and ϕ (the angle between the rebar center and the antenna center). ϕ is calculated via (2) and the depth and position of point O', h and x_0, are obtained via (3) and (4).

$$d = \sqrt{\left(x - x_T - \frac{\delta x}{2}\right)^2 + (y + r)^2} - r \tag{1}$$

$$\phi = \arctan \frac{x - \left(x_T + \frac{\delta x}{2}\right)}{y + r} \tag{2}$$

$$h = y + r(1 - \cos\phi) \tag{3}$$

$$x_0 = x - r \sin\phi \tag{4}$$

Finally, d_T and d_R are calculated using (5) and (6), respectively. Considering the medium around the rebar to be homogeneous with relative permittivity ϵ, the two-way travel time of the EM pulse diffracted from rebar, $t_{TO'R}$, is obtained from (7), where c is the speed of light in free space and t_0 is the effective time zero at which the pulse leaves the transmitter.

$$d_T = \sqrt{(x_0 - x_T)^2 + h^2} \tag{5}$$

$$d_R = \sqrt{\left(x_0 - xT - \frac{\delta x}{2}\right)^2 + h^2} \tag{6}$$

$$t_{TO'R} = \frac{d_T + d_R}{c/\sqrt{(\epsilon)}} + t_0 \tag{7}$$

2.2. Parameter estimation, ray-based analysis

The rebar diameter and location can thus be calculated by finding the radius, position, and concrete permittivity that best fit the ray travel times in Eq. (7). However, the accuracy of this method is still limited, due to its inherent limitations in accounting for the interaction of finite bandwidth 3D pulses with scattering objects. Additional errors arise if data are noisy or if hyperbola picking is performed inaccurately [6,7].

2.3. Parameter estimation, FWI

The imperfect ray-based estimates are thus used here as the initial estimates for the FWI process. We note that full waveform inversion also requires an initial estimate of the concrete conductivity, and the rebar permittivity and conductivity. The initial concrete conductivity estimate is derived with the method of [7]. The FWI process involves iterations with forward modeling of the wave propagation, which is done using the code gprMax [33]. The rebar is fixed as "pec", or perfect electric conductor, in gprMax. The radar wave does not penetrate this medium and hence the medium does not have defined material properties. (We note that this

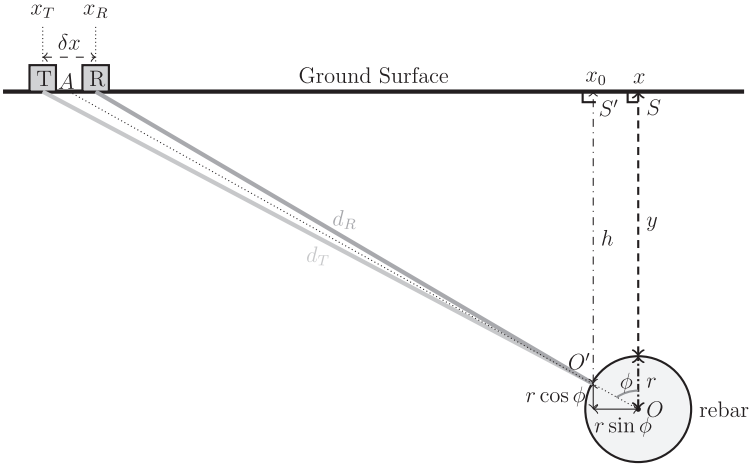

Fig. 2. Geometry for cylinder detection using ground-coupled common-offset GPR antennas. The cylinder size is exaggerated for clarity.

assumption would not be appropriate for corroded rebars.) The initial estimates of all other properties are updated in the FWI process.

Because the FWI process aims to find the model that best fits the real data, the shape of the transmitted pulse must be considered. The effective pulse shape, or source wavelet, cannot be directly measured for ground-coupled antennas. Deconvolution strategies offer an alternative solution. Deconvolution methods that require no initial information of subsurface geometry are known as blind deconvolution. Recent developments in blind deconvolution enable us to handle even noisy data based on a sparsity assumption of subsurface reflectivities. Here we use the sparse blind deconvolution (SBD) algorithm from Jazayeri et al. [30], described briefly below.

Data can be considered as a convolution product of the source wavelet and the subsurface reflectivity model, both unknown, plus additive noise. Fully blind deconvolutions that can solve for both unknowns are extremely computationally expensive. However if an initial estimate for the source wavelet can be captured from the data, the sparse reflectivity model can be estimated using an $\ell_2 - \ell_1$ norm problem solved by Split-Bregman algorithms (e.g. [30]). This process then can be taken into a two-step loop of updating the SW (by solving an $\ell_2 - \ell_2$ norm problem, the Wiener filter) and then the reflectivity model. If sufficient care is taken while selecting the initial SW, the final SW and reflectivity models are likely to be the global solutions for this minimization problem. (This requirement is loosely equivalent to a starting model in which the pulses differ by less than half a wavelength from the true values [34].) The final SW is fed into the FWI process.

The final reflectivity structure that comes out of the SBD can be considered as a model of data in which the effect of the pulse shape and much of the noise are removed. Therefore, the hyperbolas in the estimated reflectivity model are clear and are used to perform the ray-based analysis associated with Eqs. (2)–(7). The ray-estimated rebar locations and diameters and concrete permittivity are used as the FWI starting model.

We evaluate the performance of the proposed method on one synthetic and two real data examples acquired with different instruments in different experiments. Data preparation for the real data sets before the FWI follows the steps listed in Jazayeri et al. [7]. These steps include a standard dewow filter and a time-zero correction, followed by a low pass filter that depends on the antenna frequency. Details on the FWI process are described in step 5 of Jazayeri et al. [7]. Here, the convergence criteria is set to 0.2%, i.e. iterations cease when the cost function value of an iteration differs by less than this fraction from the previous iteration. The Split Bregman parameter value selection follows the recommendations in Jazayeri et al. [30].

2.4. Material

2.4.1. Synthetic model, reinforced concrete

For the synthetic test, we use gprMax to create 3D data with the derivative of a Ricker wavelet with 35° phase rotation as the source wavelet (following [30,7]). The antenna is a Hertzian dipole with 3 cm transmitter-receiver offset and nominal frequency of 2.4 GHz. Four metallic rebars are placed at depths between 2.7 and 4 cm (see Table 1 and Fig. 3) in uniform concrete. Noise is added to the data with a Gaussian distribution of high-frequency noise centered at 3 GHz and peak value of 25% of the pulse amplitude, and lower frequency noise (1.5 MHz) added at a lower level (15% of pulse amplitude) (Fig. 1).

2.4.2. Real scenario, case 1

A concrete block with length 137 cm, width 25 cm and depth 15 cm was constructed using normal weight concrete ($\frac{water}{cement}$ ratio of 0.4; maximum aggregate size of 19 mm with a 28 day target compressive strength of 4000 psi) (Fig. 6) [14]. Three different standard 19 mm ($\frac{3}{4}''$) rebars were embedded with different concrete covers (2.5, 5, 7.5 cm) (Fig. 7). A ground-coupled 2.6 GHz GSSI system was used to collect GPR B-scans perpendicular to the direction of the bars. The low-pass filter cutoff, applied to the data before further processing, was set to 3.2 GHz.

Table 1
The true, ray-based estimated and FWI-estimated parameter values for the synthetic model shown in Figs. 1, 3, and 4. x represents the bar horizontal location in cm, y the depth in cm and d the diameter in mm. ϵ is the unit-less concrete relative permittivity and σ is the concrete conductivity in mS/m. Error represents the error in the estimate of the bar diameter.

rebar#	True			Ray-based				FWI			
	x	y	d	x	y	d	error	x	y	d	error
1	15	3.5	20	16.5	4.6	24.9	24.5%	14.9	3.6	21.63	8.15%
2	35	3.5	20	36.5	4.1	7.2	64%	35.0	3.5	19.02	4.9%
3	60	4	20	61.5	5.9	44.8	124%	60.0	3.8	16.95	15.25%
4	80	2.7	20	81.4	3.9	35.7	78.5%	78.0	2.5	22.31	11.55%

Parameter	True	Ray-based	FWI
$\bar{\epsilon}_{concrete}$	5	3.89	4.77
$\sigma_{concrete}$	10	14.2	11.2

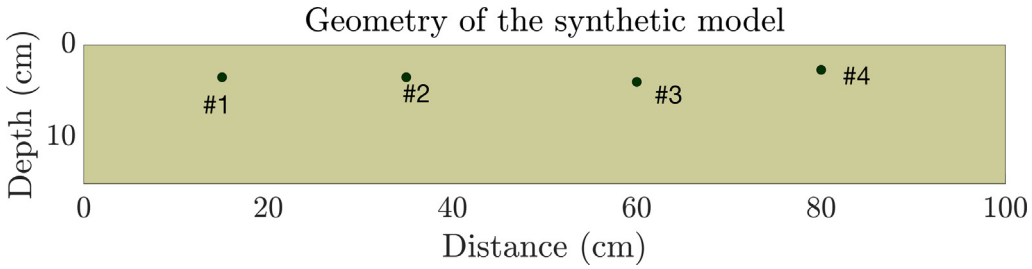

Fig. 3. Cross section of the 3D geometry model for rebars in homogeneous concrete. Four bars are simulated at varying depths.

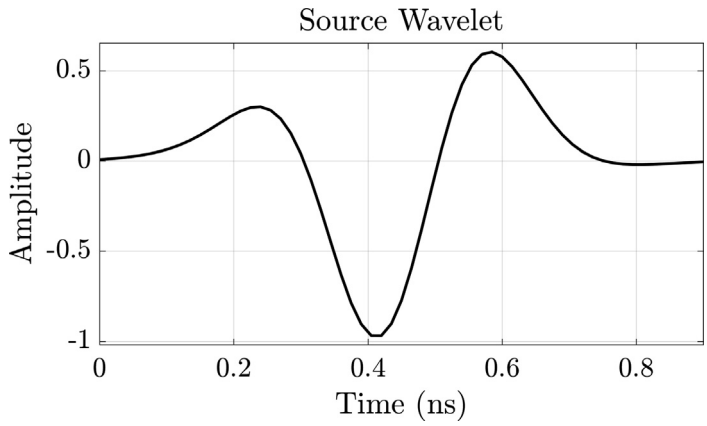

Fig. 4. The source wavelet used to create the synthetic GPR data in Fig. 1 from the model in Fig. 3 is a Ricker wavelet derivative with 35° phase rotation.

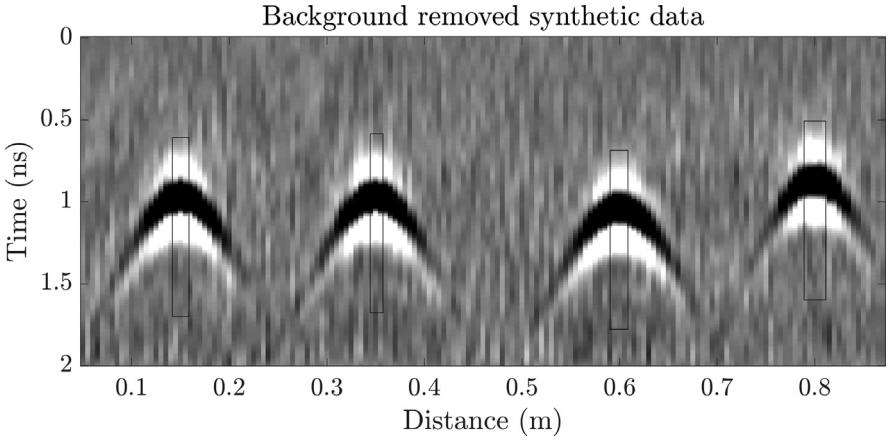

Fig. 5. Synthetic data from Fig. 1 after background removal to eliminate the direct wave. Black boxes show sections of the data used to define the initial source wavelet for the sparse blind deconvolution.

Fig. 6. Real data – case 1: Construction of the concrete box with three 19-mm reinforcing bars at depths ranging from 2.5 to 7.5 cm.

2.4.3. Real scenario, case 2

Along with other objects (PVC pipes and a tennis ball), seven 10 mm rebar were embedded in a concrete slab, each at a different depth (Fig. 9 and Table 3). Compared to the experiment in case 1, these rebar are approximately half the dimension, and buried over a greater depth range, from 0.5 to 15 cm. A common-offset B-scan was collected using the Noggin 1000 Sensors and Software system with 1 GHz nominal frequency perpendicular to the rebar direction (Fig. 10). The low-pass filter cutoff, applied to the data before further processing, was set to 1.6 GHz. Unlike the case 1 study, the hyperbolas overlap one another at their outer edges.

3. Results

3.1. Synthetic data, reinforced concrete

Parts of the diffracted signal are mixed with the direct waves, especially for the rebar #4 (Fig. 1). Realistic modeling of the direct wave is challenging due to the fact that it falls in the near-field zone. To avoid including the direct wave in the analysis, an average trace removal is applied across the whole profile (Fig. 5).

To define the initial source wavelet required for the SBD algorithm sections of data in proximity to the hyperbola apexes are carefully selected, time-shifted in order to maximize the zero-lag

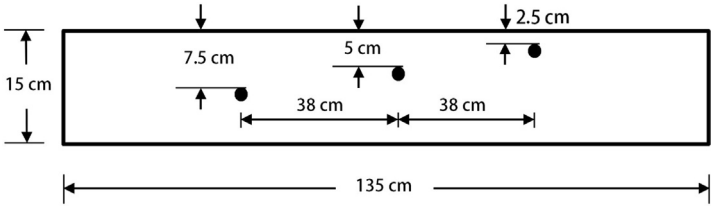

Fig. 7. Real data – case 1: Schematic cross section of the experimental geometry shown in Fig. 6. Three 19-mm bars are embedded at different depths.

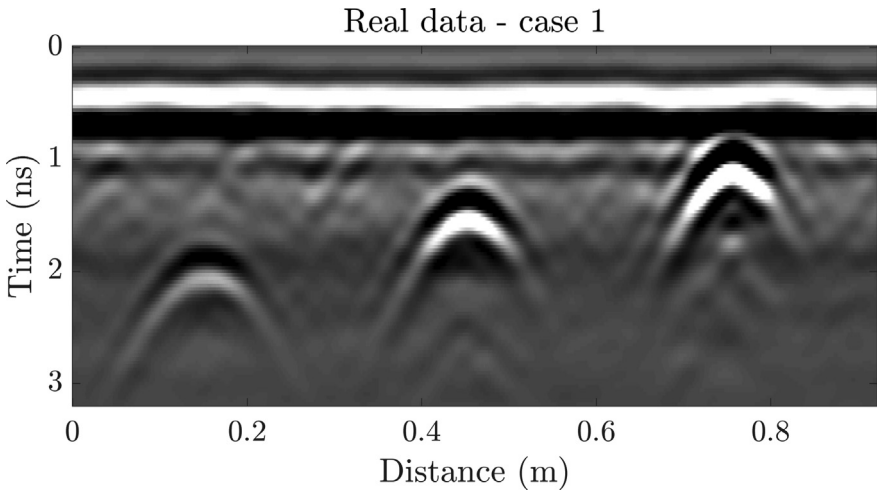

Fig. 8. Real data – case 1, GPR profile (B-scan) from a 2.6 GHz antenna over the experiment shown in Fig. 7. The three bars each produce a distinctive hyperbolic return.

Fig. 9. Real data – case 2: Construction of the concrete box with seven 10-mm reinforcing bars at depths ranging from 0.5 to 15 cm. (Photos courtesy of Sensors & Software Inc.)

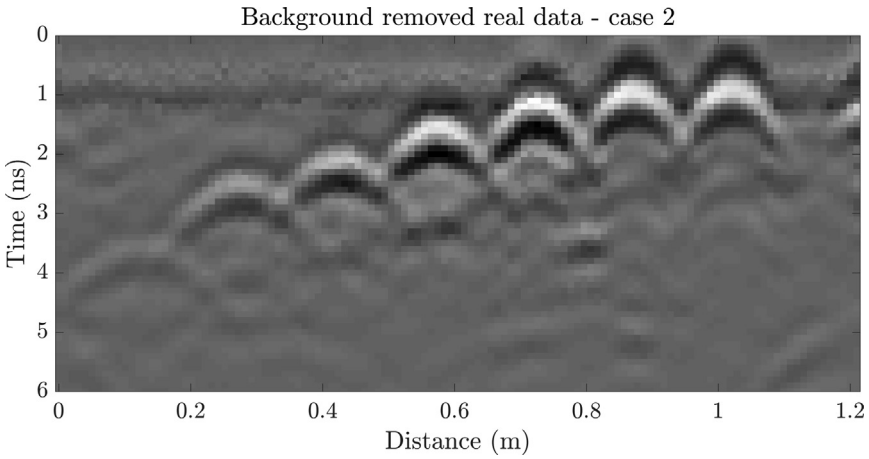

Fig. 10. Real data – case 2. GPR B-scan with 1 GHz antenna over seven rebar from 15 to 0.5 cm depth shown in Fig. 9. Background removal is applied to mute the direct wave.

cross-correlation, stacked and normalized (black boxes on Fig. 5). This results in an initial wavelet whose general shape follows the true wavelet, but the amplitudes of the two positive parts of the signal are clearly under-estimated (Fig. 11 top). The SBD process successfully modifies this initial wavelet to a wavelet closer to the true one, although some mismatch remains, presumably due to the effects of noise in the data. The final estimated reflectivity model (Fig. 11 bottom) is a relatively clean representation of the data with the source wavelet removed. The hyperbolic portions of the reflectivity model are then used for the ray-based analysis to determine the initial model. At this stage horizontal locations of the targets are well estimated. However from the ray-based analysis alone, significant errors remain in the estimates of the rebar depth, relative permittivity and conductivity of the concrete, and especially the rebar diameters (Table 1). On average, the diameter values are estimated with 73% error, with a minimum of 25% and a maximum of 124% error.

The FWI process then improves the estimates of almost all parameters, particularly the diameter values (Table 1). Convergence criteria are met after 14 iterations (Fig. 12). The average error in the diameter after FWI is 9.7%, with a minimum of 4% and maximum of 15.2%. Since the FWI estimate for $\varepsilon_{concrete}$ is improved over the ray-based value, depths are also more accurately estimated. The concrete conductivity estimate is similarly improved.

3.2. Real data, case 1

As for the synthetic example, the returns from the shallowest rebar (thinnest cover thickness) are mixed in the direct wave (Fig. 8) so background removal is applied before SBD (Fig. 13). The initial source wavelet for SBD is captured from the data (black boxes in Fig. 13). The SBD process alters the shape of the initial wavelet, especially around the tail (Fig. 14 top). The estimated reflectivity model used to define the initial model for the FWI is shown in Fig. 14 bottom. From the ray-based analysis, the diameter values are estimated with 35% error, with a minimum of 25% and a maximum of 44% (Table 2).

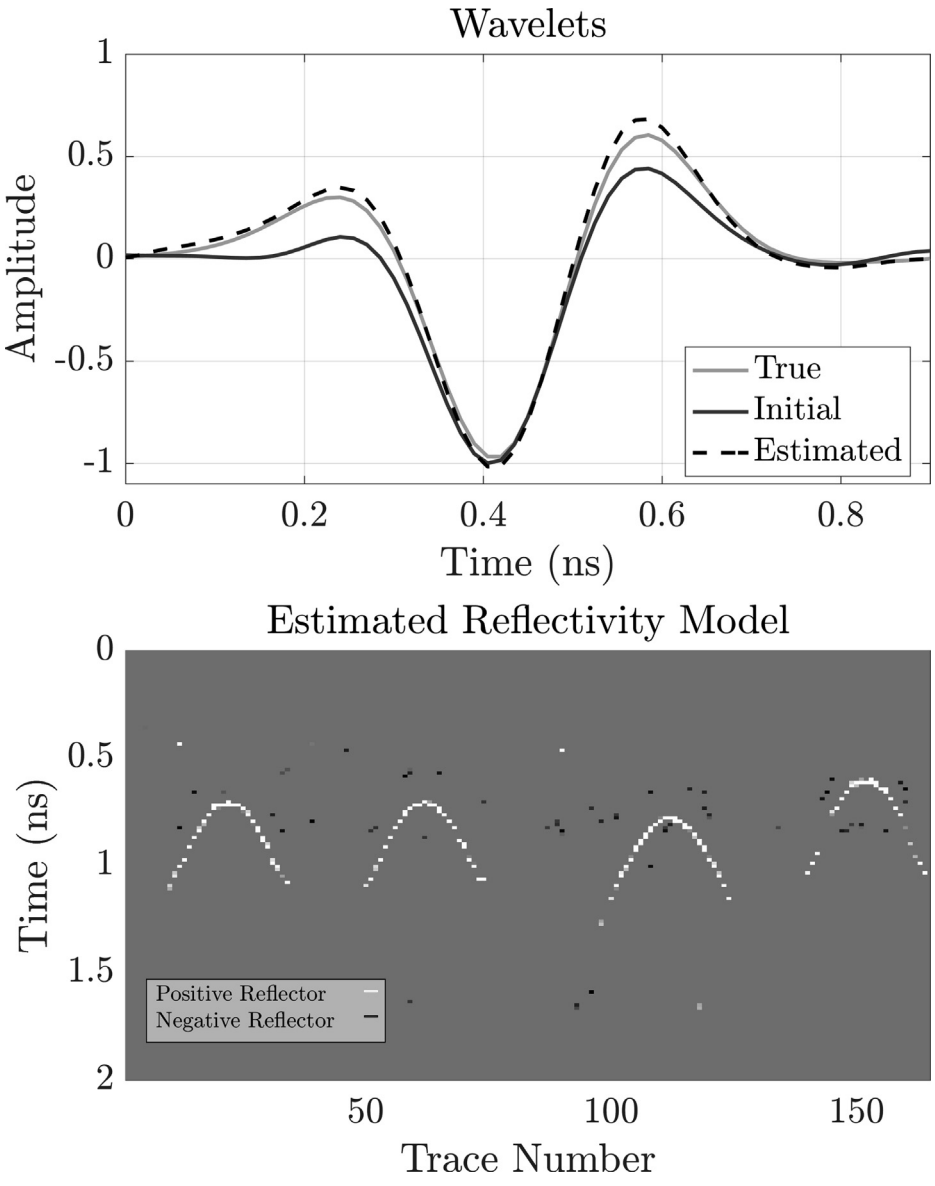

Fig. 11. Top. True source wavelet from the synthetic model (solid gray line); initial source wavelets estimated from the wavelets captured in the boxes shown in Fig. 5 (solid black line); and source wavelet estimated from the SBD (dashed black line). Bottom. The estimated reflectivity model of the synthetic data from the SBD. The reflectivity model contains a range of values, the color scale has been flattened for clarity.

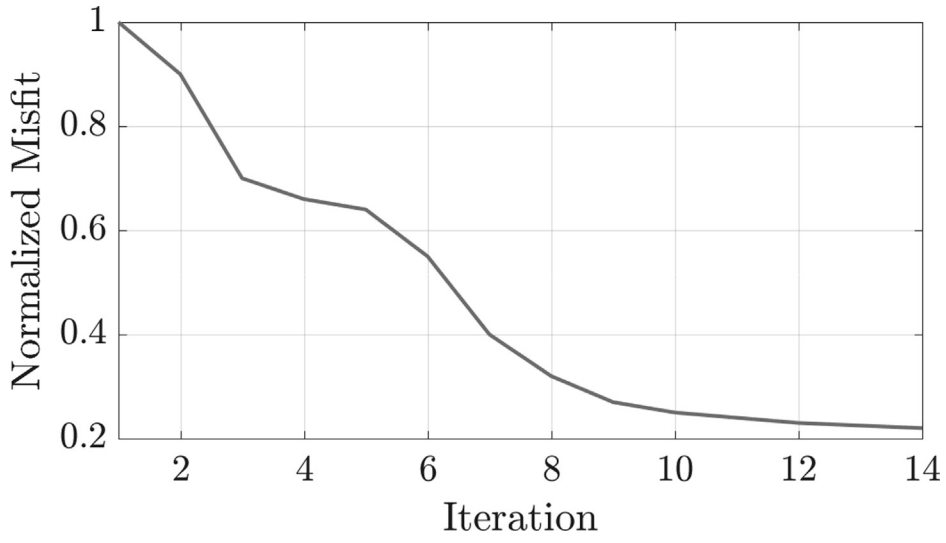

Fig. 12. The FWI misfit curve as a function of iteration for the synthetic model (see Figs. 1, 3, 4, 5, 11). The FWI process converges after 14 iterations. (Convergence is defined when misfit change < 0.2%.)

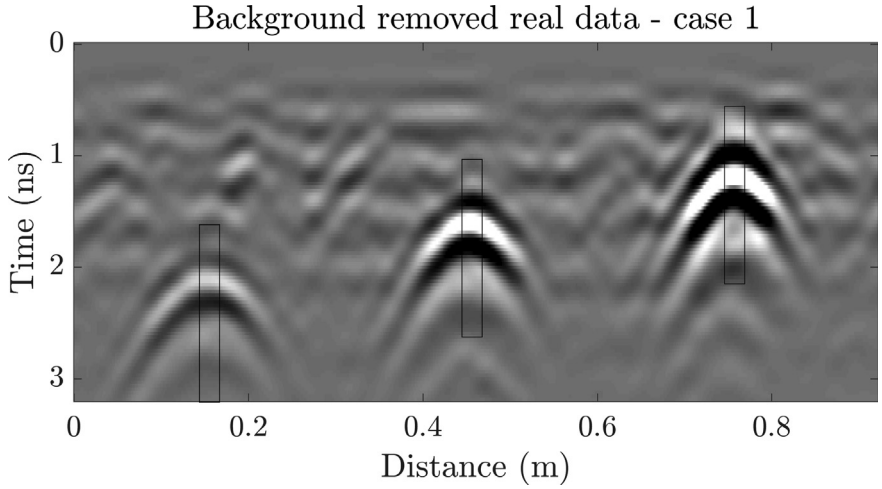

Fig. 13. Real data – case 1 (as in Fig. 8) with background removed. Black boxes show sections of the data used to define the initial source wavelet for the SBD.

The FWI process reaches convergence after 21 iterations (Fig. 15). Errors in diameter estimates are significantly reduced, as shown in Table 2. The average error for the estimated diameter values after FWI is 7.2%, with a minimum of 0.1% and a maximum of 11.1%. FWI simultaneously improves estimates of rebar depths, presumably due to a better $\varepsilon_{concrete}$ estimation. The conductivity estimate is also altered significantly (Table 2).

3.3. Real data, case 2

As for the previous test cases, the wavelet is carefully captured from the data and optimized through the SBD to estimate the source wavelet. The reflectivity model estimated from SBD is similarly used for the ray-based analysis. FWI convergence is achieved after 25 iterations (Fig. 17). The ray-based and final FWI results are included in Table 3. On average the sizes estimated with the ray-based analysis have 61% error with a minimum of 30% and maximum of 162% error. After the FWI process the average size estimation error is 17% with a minimum of 3% and a maximum of 51% error. The highest errors are found for the deepest targets where amplitudes are lower and signal to noise ratio is poorest.

4. Discussion

The improvements in estimates of rebar diameter and depth below surface achieved with FWI are summarized in Fig. 18. Each arrow represents the net change in parameter space resulting from the application of the FWI, starting from the ray-based results. The corresponding circle near the arrow tip represents the true values. Fig. 18 shows (a) FWI improves both rebar location and dimension estimates in every case, but the improvement is much more significant for diameter estimate than depth; (b) the ray-based starting modeling and FWI results are both poorest for deepest rebar (10–15 cm); and (c) after FWI the depth to rebar is least well estimated for the shallowest rebar (0.5 cm), presumably due to incomplete accounting of near-field effects. In all cases the FWI process iterates toward a better estimate of the diameter, but stops short of the true value global minimum. This suggests modifications to convergence criteria could potentially improve these results

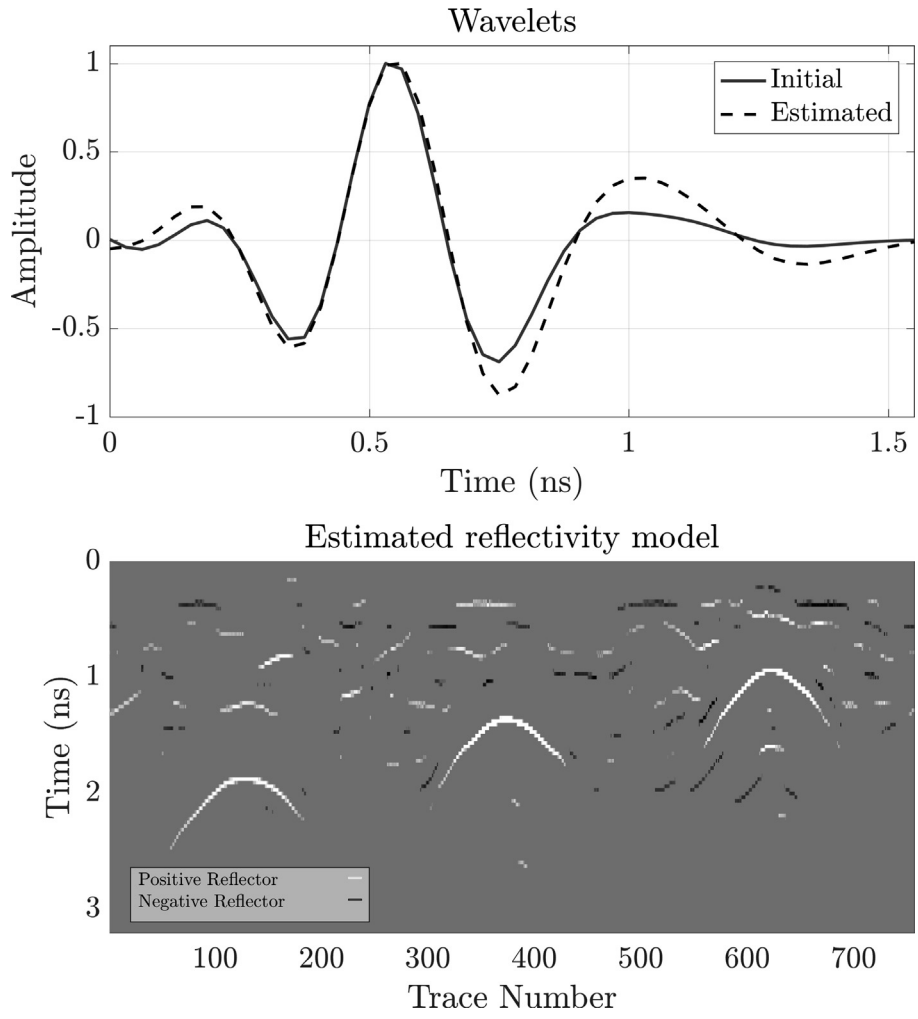

Fig. 14. Real data – case 1: Top. Initial source wavelet estimated from the data in the boxes shown in Fig. 13 (solid black line); source wavelet estimated from the SBD (dashed black line) for the 2.6 GHz antenna. Bottom. The estimated reflectivity model from the SBD.

Table 2
Real data – case 1 (see Figs. 6,7,8, 13). The true, ray-based and FWI-estimated parameter values for the experimental data collected using a 2.6 GHz antenna. x represents the horizontal location in cm, y the depth in cm and d the diameter in mm. ϵ is unit-less concrete relative permittivity and σ is concrete conductivity in mS/m. Error represents the error in the estimate of the bar diameter.

rebar#	True			Ray-based				FWI			
	x	y	d	x	y	d	error	x	y	d	error
1	15	2.5	19	15.3	2.2	14.3	24.7%	15.0	2.4	17.0	10.4%
2	45	5.0	19	44.5	4.1	27.3	43.9%	45.0	5.0	19.0	0.1%
3	76	7.5	19	74.4	6.9	12.0	36.8%	75.5	7.6	16.8	11.1%

Parameter	True	Ray-based	FWI
$\bar{\epsilon}_{concrete}$	–	5.11	4.77
$\sigma_{concrete}$	–	8.22	14.09

(a topic beyond the scope of this paper). Finally, Fig. 18 illustrates that results depend on the data quality: the traces recorded in case 1 (shown in red-themed) were noisier than those recorded in case 2 (shown in gray-themed). The noisy data results in both poorer starting models and poorer post-FWI results for rebar at comparable depths, despite the fact that case 1 involves a higher-frequency antenna over larger-diameter reinforcing bars.

Overall, the errors in the FWI estimates of rebar diameters are similar to values reported for other methods (6–12%) employing cross-polarized antennas, or ancillary methods. Relative to these other methods FWI has the advantage of requiring only the standard co-polarized antenna configuration and only GPR data, but it has disadvantage of requiring significant post-acquisition computations.

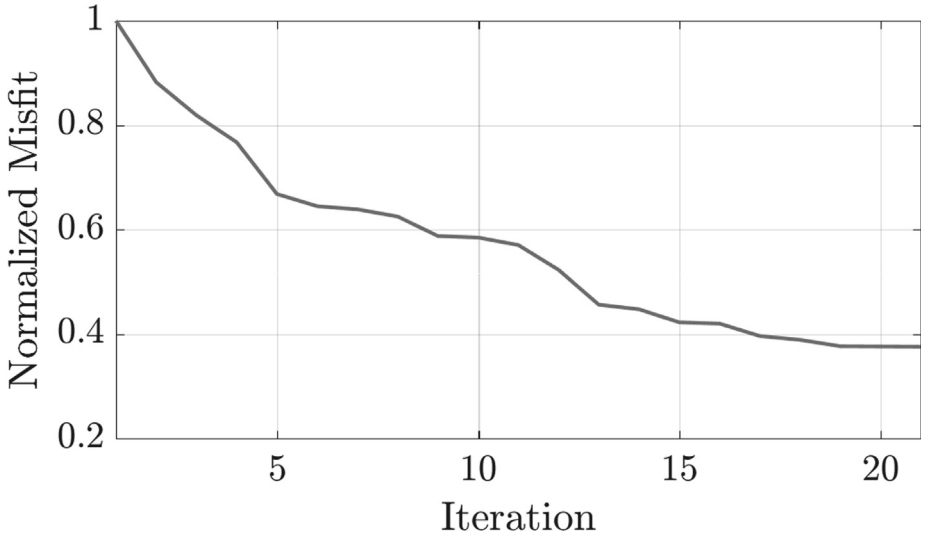

Fig. 15. The FWI misfit curve as a function of the iterations for the real data, case 1 (Figs. 6,7,8, 13, 14). The FWI process converges to the minima after 21 iterations. (Convergence is defined when misfit change <0.2%.)

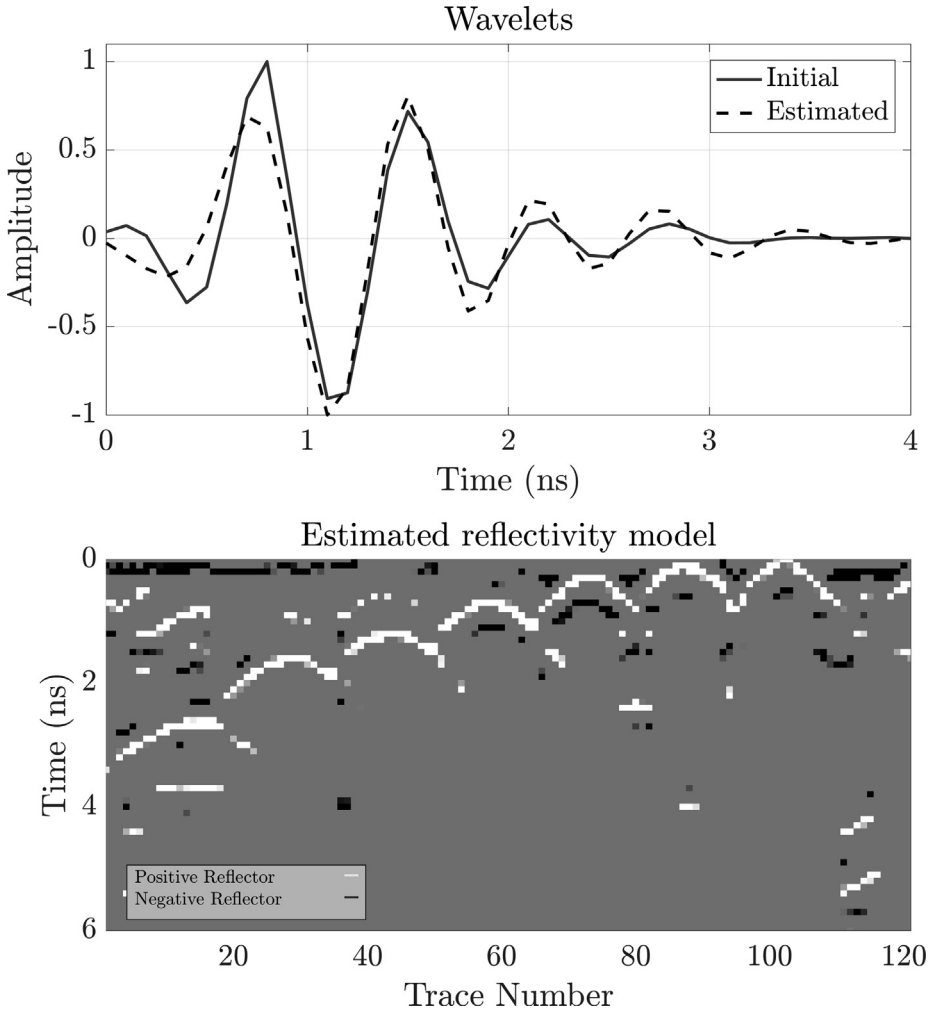

Fig. 16. Real data – case 2: Top. Initial source wavelet estimated from the data (solid black line); source wavelet estimated from the SBD (dashed black line) for the 1 GHz antenna. Bottom. The estimated reflectivity model from the SBD.

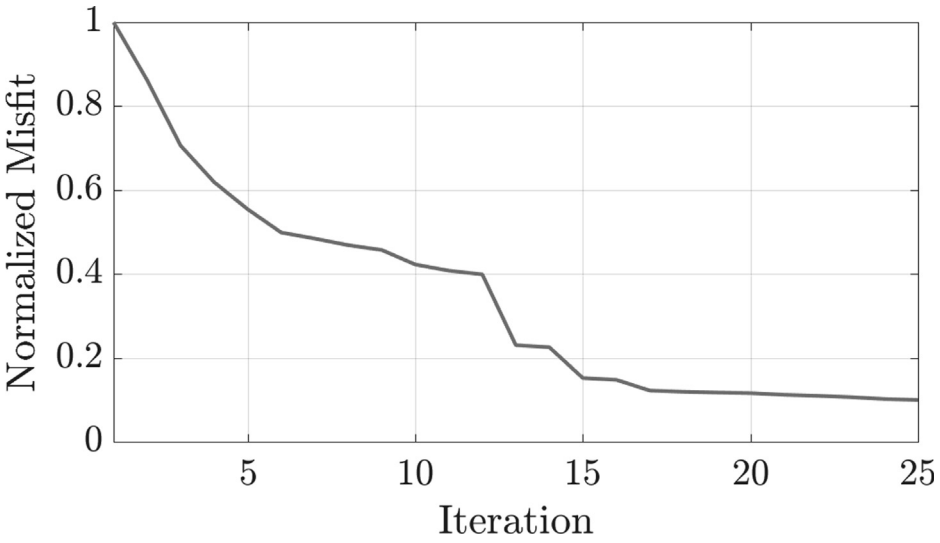

Fig. 17. The FWI misfit curve as a function of for the real data, case 2 (Figs. 9, 10, 16). The FWI process converges after 25 iterations. (Convergence is defined when misfit change <0.2%.)

Table 3
Real data – case 2 (see Figs. 9, 10, 16, 17, 18). True and estimated parameter values for the experimental data collected using a 1 GHz antenna. Rebar numbers start from the left side of the concrete slab shown in Fig. 9. x represents the horizontal location in cm, y the depth in cm and d the diameter in mm. ϵ is unit-less concrete relative permittivity and σ is concrete conductivity in mS/m. Error represents the error in the estimate of the bar diameter.

rebar#	True			Ray-based				FWI			
	x	y	d	x	y	d	error	x	y	d	error
1	15	15	10	14.9	16.8	26.2	162%	14.9	14.6	15.1	51%
2	30	10	10	29	9.4	17.7	77%	29.5	9.8	12.8	28%
3	45	7.5	10	45.1	8.2	14.2	42%	45.1	7.6	9.7	3%
4	60	5	10	60	5.5	13.0	30%	60	5.2	10.3	3%
5	75	2.5	10	75.4	3.1	5.5	45%	75.3	2.6	8.9	11%
6	90	1	10	89.7	0.5	15.1	51%	90	0.9	10.4	4%
7	105	0.5	10	104.9	0.0	15.9	59%	105.1	0.2	10.6	6%

Parameter	True	Ray-based	FWI
$\bar{\epsilon}_{concrete}$	–	6.56	5.98
$\sigma_{concrete}$	–	28.45	19.72

All examples reported here assume uniform permittivity and conductivity in the concrete. The synthetic case demonstrates that the FWI improves estimates of both these parameters, as has been demonstrated in other forms by Kalogeropoulos et al. [11,12].

We note that concrete properties are sensitive to corrosion, and thus the problems of detecting bar diameter and corrosion are necessarily intertwined, as measured GPR returns depend on both the concrete they travel through and the rebars. Lai et al., [13], Hasan and Yazdani [14] and Martino et al. [35] report that the travel times, amplitudes, and frequency spectra of GPR returns change as corrosion progresses. Concrete deterioration effects can furthermore be linked with changes in a rebar diameter as it undergoes macrocell corrosion. However, significant deterioration (e.g. cracking, delamination) can occur in association with very small (less than 1 mm per year [36]) increases in bar diameter. The results of this paper are thus relevant only to resolving diameter for scenarios in which the dimensions of embedded bars are unknown, rather than resolving very small diameter changes associated with corrosion.

5. Conclusions

We provide the mathematical expressions for cylindrical targets in common-offset GPR data assuming non-point diffractors and realistic antenna offset, in order to optimize estimates of cylindrical target diameter using ray-based analysis. Travel times for the ray-based analysis are estimated from the reflectivity series derived from a sparse blind deconvolution of the radar data. Output parameters from the ray-based analysis and an effective source wavelet estimated from the same deconvolution are used to create a starting model for full-waveform inversion of the radar data on reinforced concrete.

For a synthetic scenario and two experiments using different instruments over rebars with concrete cover ranging from 0.5 to 15 cm thickness, the FWI significantly improves estimates of rebar diameters over the ray-based analyses. Errors in the final diameter estimates range from 0.1% to 11% for scenarios where the bar depth is 7.5 cm or less.

A key limitation in the method presented here is that it requires the GPR profile to be perpendicular to the rebars. Errors associated

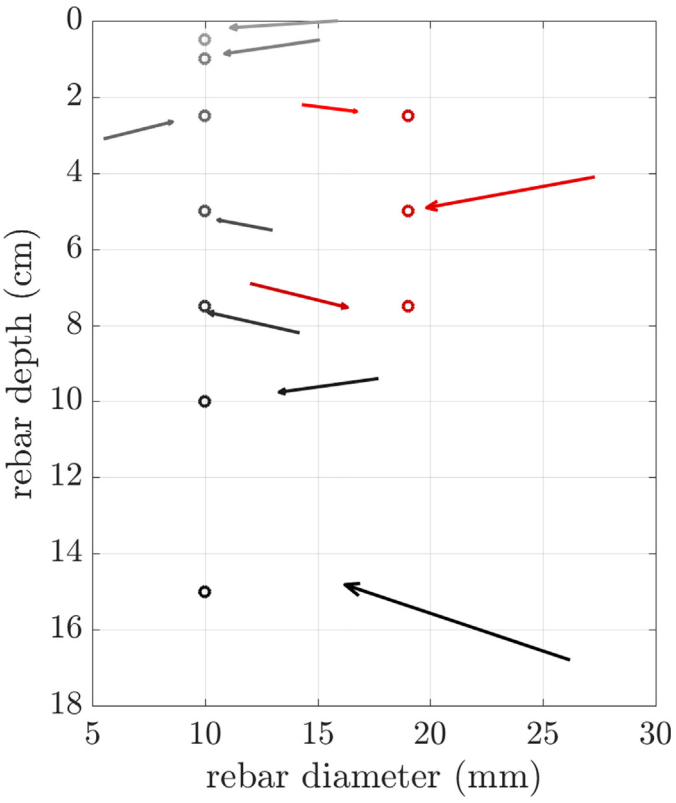

Fig. 18. Summary of improvements achieved with FWI for experimental data cases listed in Tables 2 and 3, case 1 (red-themed colors) and 2 (gray-themed colors) respectively. The tail of each arrow represents the starting depth and diameter parameters derived from the ray-based analysis; the tip of each arrow represents the values after FWI convergence (as in Figs. 15 and 17). The dot near the tip of each arrow represents the true experimental values. See text for discussion. (For interpretation of the references to colour in this figure legend, the reader is referred to the web version of this article.)

with this assumption are the topic of future investigation. Future research will also consider the effects of heterogeneity in the overlying concrete and relationships to corrosion status.

Declaration of Competing Interest

The authors report no conflict of interest.

Acknowledgments

The authors are grateful to Nectaria Diamanti for constructive comments and Greg Johnston and Sensors & Software Inc. for sharing the data in case 2. Tariq Alkhalifah and an anonymous reviewer provided very constructive comments that improved the manuscript.

References

[1] A. Benedetto, L. Pajewski, Civil Engineering Applications of Ground Penetrating Radar, Springer, 2015.
[2] A. Annan, Ground-penetrating radar, in: Near-Surface Geophysics, Society of Exploration Geophysicists, 2005, pp. 357–438.
[3] I. Al-Qadi, S. Lahouar, Part 4: Portland cement concrete pavement: measuring rebar cover depth in rigid pavements with ground-penetrating radar, J. Transp. Res. Board 2005 (1907) 80–85.
[4] J. Hugenschmidt, A. Kalogeropoulos, F. Soldovieri, G. Prisco, Processing strategies for high-resolution GPR concrete inspections, NDT & E Int. 43 (4) (2010) 334–342.
[5] A.M. Alani, M. Aboutalebi, G. Kilic, Applications of ground penetrating radar (GPR) in bridge deck monitoring and assessment, J. Appl. Geophys. 97 (2013) 45–54.
[6] J.F. Sham, W.W. Lai, Development of a new algorithm for accurate estimation of GPR's wave propagation velocity by common-offset survey method, NDT & E Int. 83 (2016) 104–113.
[7] S. Jazayeri, A. Klotzsche, S. Kruse, Improving estimates of buried pipe diameter and infilling material from ground-penetrating radar profiles with full-waveform inversion, Geophysics 83 (4) (2018) H27–H41, https://doi.org/10.1190/geo2017-0617.
[8] F. Soldovieri, R. Solimene, L.L. Monte, M. Bavusi, A. Loperte, Sparse reconstruction from GPR data with applications to rebar detection, IEEE Trans. Instrum. Meas. 60 (3) (2011) 1070–1079.
[9] F. Soldovieri, R. Persico, E. Utsi, V. Utsi, The application of inverse scattering techniques with ground penetrating radar to the problem of rebar location in concrete, NDT & E Int. 39 (7) (2006) 602–607.
[10] M.I. Hasan, N. Yazdani, An experimental and numerical study on embedded rebar diameter in concrete using ground penetrating radar, Chin. J. Eng. (2016).
[11] A. Kalogeropoulos, J. Van der Kruk, J. Hugenschmidt, S. Busch, K. Merz, Chlorides and moisture assessment in concrete by gpr full waveform inversion, Near Surf. Geophys. 9 (3) (2011) 277–285.
[12] A. Kalogeropoulos, J. Hugenschmidt, J. van der Kruk, J. Bikowski, E. Brühwiler, Gpr full-waveform inversion of chloride gradients in concrete, in: 2012 14th International Conference on Ground Penetrating Radar (GPR), 2012, pp. 320–323, https://doi.org/10.1109/ICGPR.2012.6254882.
[13] W.-L. Lai, T. Kind, M. Stoppel, H. Wiggenhauser, Measurement of accelerated steel corrosion in concrete using ground-penetrating radar and a modified half-cell potential method, J. Infrastruct. Syst. 19 (2) (2012) 205–220.
[14] M.I. Hasan, N. Yazdani, An experimental study for quantitative estimation of rebar corrosion in concrete using ground penetrating radar, J. Eng. (2016).
[15] V. Utsi, E. Utsi, Measurement of reinforcement bar depths and diameters in concrete, in: Ground Penetrating Radar, 2004. GPR 2004. Proceedings of the Tenth International Conference on, IEEE, 2004, pp. 659–662.
[16] G. Leucci, Ground penetrating radar: an application to estimate volumetric water content and reinforced bar diameter in concrete structures, J. Adv. Concr. Technol. 10 (12) (2012) 411–422.
[17] L. Zanzi, D. Arosio, Sensitivity and accuracy in rebar diameter measurements from dual-polarized GPR data, Constr. Build. Mater. 48 (2013) 1293–1301.
[18] V. Barrile, R. Pucinotti, Application of radar technology to reinforced concrete structures: a case study, NDT & E Int. 38 (7) (2005) 596–604.
[19] R.G. Pratt, C. Shin, G. Hick, Gauss–newton and full newton methods in frequency–space seismic waveform inversion, Geophys. J. Int. 133 (2) (1998) 341–362.
[20] J. Virieux, S. Operto, An overview of full-waveform inversion in exploration geophysics, Geophysics 74 (6) (2009) WCC1–WCC26.
[21] R. Brossier, Two-dimensional frequency-domain visco-elastic full waveform inversion: parallel algorithms, optimization and performance, Comput. Geosci. 37 (4) (2011) 444–455.
[22] T. Alkhalifah, R.-É. Plessix, A recipe for practical full-waveform inversion in anisotropic media: an analytical parameter resolution study, Geophysics 79 (3) (2014) R91–R101.
[23] K.T. Tran, D.R. Hiltunen, Two-dimensional inversion of full waveforms using simulated annealing, J. Geotech. Geoenviron. Eng. 138 (9) (2011) 1075–1090.
[24] K.T. Tran, M. McVay, M. Faraone, D. Horhota, Sinkhole detection using 2d full seismic waveform tomographysinkhole detection by fwi, Geophysics 78 (5) (2013) R175–R183.
[25] P. Jiang, D.R. Hiltunen, A new borehole tool for subsurface seismic imaging–a full waveform inversion approach, in: IFCEE, 2015, pp. 1971–1980.
[26] T.D. Nguyen, K.T. Tran, N. Gucunski, Detection of bridge-deck delamination using full ultrasonic waveform tomography, J. Infrastruct. Syst. 23 (2) (2016) 04016027.
[27] H. Wang, A. Che, S. Feng, Quantitative investigation on grouting quality of immersed tube tunnel foundation base using full waveform inversion method, Geotech. Test. J. 40 (5) (2017) 833–845.
[28] S. Jazayeri, S. Kruse, Full-waveform inversion of ground-penetrating radar (gpr) data using pest (fwi-pest method) applied to utility detection, in: SEG Technical Program Expanded Abstracts 2016, Society of Exploration Geophysicists, 2016, pp. 2474–2478, https://doi.org/10.1190/segam2016-13878165.1.
[29] T. Liu, A. Klotzsche, M. Pondkule, H. Vereecken, Y. Su, J. van der Kruk, Radius estimation of subsurface cylindrical objects from ground-penetrating-radar data using full-waveform inversion, Geophysics 83 (6) (2018) H43–H54.
[30] S. Jazayeri, N. Kazemi, S. Kruse, Sparse blind deconvolution of ground penetrating radar data, IEEE Trans. Geosci. Remote Sens. (2019) 1–10, https://doi.org/10.1109/TGRS.2018.2886741.
[31] W. Al-Nuaimy, S. Shihab, A. Eriksen, Data fusion for accurate characterisation of buried cylindrical objects using GPR, Ground Penetrating Radar, 2004. GPR 2004. Proceedings of the Tenth International Conference on, vol. 1, IEEE, 2004, pp. 359–362.
[32] S. Shihab, W. Al-Nuaimy, Radius estimation for cylindrical objects detected by ground penetrating radar, Subsurface Sens. Technol. Appl. 6 (2) (2005) 151–166.
[33] C. Warren, A. Giannopoulos, I. Giannakis, gprmax: Open source software to simulate electromagnetic wave propagation for ground penetrating radar, Comput. Phys. Commun. 209 (2016) 163–170.

[34] G.A. Meles, J. Van der Kruk, S.A. Greenhalgh, J.R. Ernst, H. Maurer, A.G. Green, A new vector waveform inversion algorithm for simultaneous updating of conductivity and permittivity parameters from combination crosshole/borehole-to-surface gpr data, IEEE Trans. Geosci. Remote Sens. 48 (9) (2010) 3391–3407.

[35] N. Martino, K. Maser, R. Birken, M. Wang, Quantifying bridge deck corrosion using ground penetrating radar, Res. Nondestr. Eval. 27 (2) (2016) 112–124, https://doi.org/10.1080/09349847.2015.1067342.

[36] B. Elsener, Macrocell corrosion of steel in concrete–implications for corrosion monitoring, Cem. Concr. Compos. 24 (1) (2002) 65–72.